

# Spin-Transfer Torque on Curved Surfaces: A Generalized Thiele Formalism

J. I. Costilla,<sup>1</sup> M. Castro,<sup>2</sup> K. V. Yershov,<sup>3,4</sup> D. Altbir,<sup>5</sup> V. L. Carvalho-Santos,<sup>1</sup> and V. P. Kravchuk<sup>3,4</sup>

<sup>1</sup>*Departamento de Física, Universidade Federal de Viçosa, Av. PH Rolfs s/n, 36570-900, Viçosa, Brazil*

<sup>2</sup>*Departamento de Física, FCFM, Universidad de Chile, Santiago, 8370448, Chile*

<sup>3</sup>*Leibniz-Institut für Festkörper- und Werkstofforschung, Helmholtzstraße 20, D-01069 Dresden, Germany*

<sup>4</sup>*Bogolyubov Institute for Theoretical Physics of the National Academy of Sciences of Ukraine, 03143 Kyiv, Ukraine*

<sup>5</sup>*Universidad Diego Portales, Cedenna, Ejército 441, Santiago, Chile*

Curvature is a highly relevant parameter when considering nanostructures, favoring the stability and affecting the dynamics of magnetic textures. In this work, we address the spin-transfer torque phenomenon by deriving an expanded Thiele equation with the Zhang-Li term for curved surfaces. Our results show a coupling between current and curvature, which is perceived as a gyrovector and an additional dissipative tensor associated with this coupling. Using this model, we determine the dynamics of a skyrmion in a nanotube with Gaussian and variable mean curvature. The new terms included in the Thiele equation are responsible for an additional Hall effect in the skyrmion dynamics and for the generalization of the Walker limit condition.

*Introduction*—The interplay between the concepts of geometry and topology provides an important framework for understanding the properties of condensed matter systems. Geometry governs local physical properties and can induce effective interactions that do not appear in flat systems. The topology classifies the global structure of an order parameter in the so-called ordered media<sup>1</sup> and confers robustness through quantized invariants<sup>2</sup>. The roles of geometry and topology are particularly important in magnetic systems. At small sizes the shape of the magnetic structure is a key point in determining its properties, giving rise to the field of curvilinear micromagnetism<sup>3–7</sup>. This discipline explores the influence of geometry on the magnetization properties of magnetic bodies embedded in three-dimensional curved architectures. In these systems, the curvature of the underlying manifold acts as a tuning parameter, directly governing the topology of the magnetization field<sup>8–12</sup>. This geometry-topology interplay enables the stabilization of non-trivial magnetic textures and triggers unconventional static and dynamic responses in curved systems that are absent in their planar counterparts<sup>13–15</sup>.

The effects of geometry on ferromagnetic systems are directly evidenced by the influence of curvature on the behavior of magnetization collective modes. For example, the number of magnetic vortices is directly determined by the Gaussian curvature of a thin magnetic shell<sup>16–19</sup>. Curvature also provides a mechanism for stabilizing skyrmions<sup>12,15,20–22</sup>, while simultaneously affecting their intrinsic properties, such as size and shape<sup>23–25</sup>. The influence of curvature extends to the dynamic properties of the magnetization by modifying the gyrovector field and the dissipative dyadic tensor<sup>21</sup>, which govern the motion of the soliton<sup>26</sup>. These curvature-induced changes give rise to different transport phenomena, including the emergence of pinning potentials<sup>21,27</sup> and a transverse drift in the skyrmion trajectory<sup>25,28</sup>.

Geometry effects extend to the current-driven dynamics of magnetic textures. In quasi-one-dimensional systems, for example, torsion and curvature modify the fundamental parameters of the spin transfer torque, effec-

tively shifting the non-adiabatic coefficient<sup>29,30</sup>. In systems with curvature gradients, the current-driven motion of a transverse domain wall generates a chiral symmetry break, where the current threshold required for the domain wall to cross the bent region depends on its propagation direction<sup>31</sup>. Although the influence of curvature on current-driven magnetic texture transport in one-dimensional structures has been extensively addressed, its analysis in 2D magnetic systems has become a new area of research. To contribute to these challenge, in this letter, by deriving a generalized Thiele equation<sup>32</sup> for curved systems, we obtain a curvature-induced renormalization of both the gyrovector and the dissipative dyadic in the current-driven term. Using a geodesic approach, we apply this model to a skyrmion propagating along a bent nanotube. These curvature-induced changes in the spin-transfer torque generate transverse-to-current displacements of the skyrmion, culminating in a curvature-driven Magnus effect of the skyrmion, even under equal Gilbert damping and non-adiabatic parameters, a regime that ensures linear trajectories in planar or cylindrical geometries. The analysis is extended to map the skyrmion dynamics on a nanotube, showing the emergence of a curvature-induced Walker-like regime for the skyrmion motion.

*Generalized Thiele formalism*— In the presence of spin-transfer torques (STT), the magnetization dynamics of a ferromagnet is governed by the Landau-Lifshitz-Gilbert equation with additional Zhang-Li torques<sup>33</sup>

$$\dot{\mathbf{m}} = \frac{\gamma}{M_s} \left[ \mathbf{m} \times \frac{\delta \mathcal{H}}{\delta \mathbf{m}} \right] + \alpha [\mathbf{m} \times \dot{\mathbf{m}}] + \mathbf{\Lambda}_u, \quad (1)$$

where a dot indicates the time derivative and  $\mathbf{\Lambda}_u = \mathbf{m} \times [\mathbf{m} \times (\mathbf{u} \cdot \nabla) \mathbf{m}] + \beta [\mathbf{m} \times (\mathbf{u} \cdot \nabla) \mathbf{m}]$  is the Zhang-Li term due to the spin-transfer torque, where the velocity parameter  $\mathbf{u} = -\mathbf{j} P \mu_B / (|e| M_s)$  is close to the drift velocity of the conductance electrons,  $\beta$  is the non-adiabaticity constant,  $\mathbf{j}$  is the density of the current with the rate of polarization  $P$ ,  $\mu_B > 0$  is the Bohr magneton, and  $e$  is the electron charge. Here,  $\mathbf{m} = \mathbf{M} / M_s$  is the

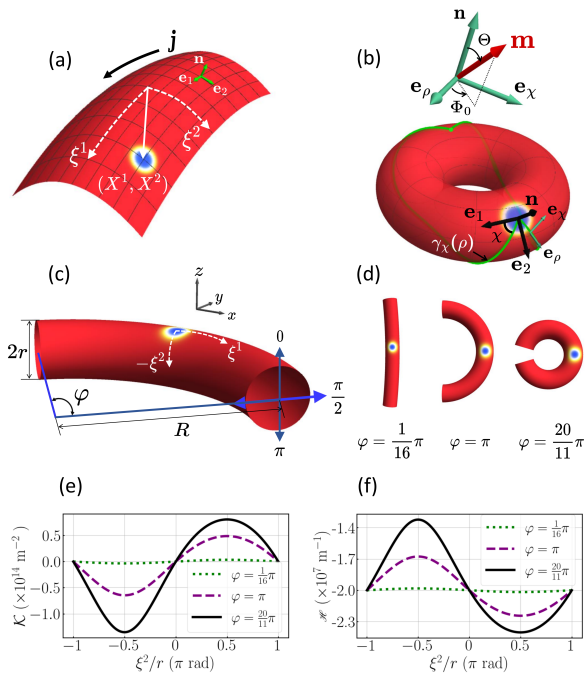


Figure 1. Geometrical framework of the curved magnetic system. (a) Curvilinear coordinate system  $(\xi^1, \xi^2)$  defining the manifold, with an inset showing the local magnetization parametrization via spherical angles. Coordinates  $X^1$  and  $X^2$  represent the position of the center of the skyrmion nucleated on the surface. (b) Diagram of a planar skyrmion profile mapped onto the curved surface. (c) Specific geometry of a bent nanotube. (d) Illustration of several nanotube opening angles and their resulting shape. (e, f) Spatial distribution of the Gaussian  $\mathcal{K}$  and mean  $\mathcal{H}$  curvatures for distinct opening angles with  $r = 50$  nm.

unit magnetization vector with  $M_s$  being the saturation magnetization,  $\gamma > 0$  is the electron gyromagnetic ratio, and  $\mathcal{H} = \int (\mathcal{E}_{\text{ex}} + \mathcal{E}_{\text{DM}} + \mathcal{E}_{\text{an}}) d\mathbf{r}$  is the total magnetic Hamiltonian of the system. In addition,  $\mathcal{E}_{\text{ex}}$ ,  $\mathcal{E}_{\text{DM}}$ , and  $\mathcal{E}_{\text{an}}$  represent the energy densities for the exchange and Dzyaloshinskii-Moriya (DM) interactions, and the easy-normal anisotropy, respectively. The parameter  $\alpha$  is the Gilbert damping constant. Note that the form of Eq. (1) is independent of the chosen reference frame.

We now consider a very thin magnetic shell parametrized as  $\mathbf{r}(\xi^1, \xi^2, \zeta) = \boldsymbol{\sigma}(\xi^1, \xi^2) + \zeta \mathbf{n}$ , where  $\boldsymbol{\sigma}(\xi^1, \xi^2)$  is the central surface of the shell with  $\xi^1$  and  $\xi^2$  being the curvilinear coordinates. Here,  $\zeta \in [-h/2, h/2]$  is the coordinate through the thickness of the shell. We assume here that the surface thickness  $h$  is much smaller than the smallest curvature radius. The surface geometry is characterized by the tangent basis vectors  $\mathbf{g}_\alpha = \partial \boldsymbol{\sigma} / \partial \xi^\alpha$ , and the associated metric tensor  $g_{\alpha\beta} = \mathbf{g}_\alpha \cdot \mathbf{g}_\beta$ , which describe the intrinsic geometry. The unit normal vector  $\mathbf{n} \equiv \mathbf{e}_1 \times \mathbf{e}_2$  defines the extrinsic orientation, as depicted in Fig. 1(a). Here,  $\mathbf{e}_\alpha = \mathbf{g}_\alpha / |\mathbf{g}_\alpha|$  are the unitary vectors. In what follows, we assume that the basis  $\{\mathbf{e}_1, \mathbf{e}_2\}$  is orthogonal and the metric tensor  $g_{\alpha\beta}$ , accord-

ingly, is diagonal.

To take advantage of the geometry, the unit magnetization vector can be locally parameterized as  $\mathbf{m}(\xi^1, \xi^2) = m^\alpha(\xi^1, \xi^2) \mathbf{e}_\alpha + m_n(\xi^1, \xi^2) \mathbf{n}$ , where the Einstein sum convention (dumb repeated index represents sums) has been adopted. Here we assume that the magnetization is uniform along the thickness, *i.e.*, it does not depend on  $\zeta$ . The STT  $\Lambda_{\mathbf{u}}$  are determined by the directional derivative  $(\mathbf{u} \cdot \nabla) \mathbf{m}$ . Assuming the tangential current  $\mathbf{u} = u^\alpha \mathbf{e}_\alpha$ , in the described curvilinear reference frame, we obtain  $(\mathbf{u} \cdot \nabla) \mathbf{m} = u^\alpha [\mathbf{e}_\beta (\nabla_\alpha m^\beta + \Omega_\alpha \epsilon_{\beta\gamma} m^\gamma - h_{\alpha\beta} m_n) + \mathbf{n} (\nabla_\alpha m_n + h_{\alpha\beta} m^\beta)] + \mathcal{O}(\zeta)$ . Here  $\nabla_\alpha = g_{\alpha\alpha}^{-1/2} \partial_\alpha$  is the gradient component,  $\Omega_\alpha = \mathbf{e}_1 \cdot \nabla_\alpha \mathbf{e}_2$  is the spin connection, and  $h_{\alpha\beta} = \mathbf{n} \cdot \nabla_\alpha \mathbf{e}_\beta$  is the shape operator also known as Weingarten map. The terms proportional to the shape operator elements generate additional driving forces resulting from the combined action of the STT and the curvature. In the same framework, one obtains curvature-induced DMI and an effective anisotropy, which are linear and quadratic in  $h_{\alpha\beta}$ , respectively<sup>13,34,35</sup>. The eigenvalues of  $h_{\alpha\beta}$  are the principal curvatures  $\kappa_1$  and  $\kappa_2$  that determine the mean  $\mathcal{H} = \kappa_1 + \kappa_2$  and the Gaussian  $\mathcal{K} = \kappa_1 \kappa_2$  curvatures.

Let us now assume that in the curvilinear reference frame  $(\xi^1, \xi^2)$ , the dynamics of the magnetic texture can be presented in the form of a traveling-wave Ansatz  $\mathbf{m} = m^\alpha(\xi^1 - X^1, \xi^2 - X^2) \mathbf{e}_\alpha + m_n(\xi^1 - X^1, \xi^2 - X^2) \mathbf{n}$ , where  $m^\alpha(\xi^1, \xi^2)$  and  $m_n(\xi^1, \xi^2)$  are known functions (e.g., the Ansatz for the skyrmion profile) and the time dependence is included in the collective coordinates  $X^\alpha = X^\alpha(t)$ , which determine the position of the magnetic pattern. Using this formalism, in the leading order in thickness  $h$  and in the linear order in principal curvatures, the extended Thiele equation including the Zhang-Li torque for the collective coordinates in a curved background is derived from Eq. (1), and is given by

$$G_{ab}(V^b - u^b) = -F_a + D_{ab}(\alpha V^b - \beta u^b) + (G_{ab}^u - \beta D_{ab}^u) u^b, \quad (2)$$

whose derivation is presented in the Supplemental Information (SI)<sup>36</sup>. Here,  $V^\alpha = \sqrt{g_{\alpha\alpha}}(X^1, X^2) \dot{X}^\alpha$  are components of the skyrmion velocity, and  $F_\alpha = -[g_{\alpha\alpha}(X^1, X^2)]^{-1/2} \partial \mathcal{H} / \partial X^\alpha$  is the curvature-induced force (CIF) acting on the skyrmion. A central finding of this work is the emergence of two distinct curvature-mediated current-driven forces: a current-curvature-induced gyrotensor (CCG,  $G_{ab}^u$ ) and a dissipative dyadic (CCD,  $D_{ab}^u$ ), whose tensorial structure is directly governed by the background curvature, revealing a fundamental coupling between spin currents, magnetization dynamics, and geometry. The gyrotensor  $G_{ab}$  and the damping tensor  $D_{ab}$  were previously obtained for curved films<sup>21</sup> hosting a skyrmion, showing that, at the limit where the curvature radii are much larger than the skyrmion size,  $G_{ab}$  and  $D_{ab}$  tend towards the values of a flat film<sup>21</sup>. It can be highlighted that the CCG and CCD vanish in the case of a flat surface, so that Equations

tion (2) coincides with the Thiele equation generalized for a stripe<sup>32</sup>.

To compute the coefficients in the generalized Thiele equation (2), we write the skyrmion Ansatz in geodesic polar coordinates (GPC) (see SI<sup>36</sup> for details). For this purpose, from the center of the skyrmion ( $X^1, X^2$ ), we launch geodesics  $\gamma_\chi(\rho)$  at different angles  $\chi$  relative to the principal direction  $\mathbf{e}_1$ , where  $\rho$  is the geodesic arc-length starting from the center of the skyrmion and  $\mathbf{e}_\rho = \partial_\rho \gamma_\chi$  is the unit vector tangential to  $\gamma_\chi$ . In the orthonormal coordinate-dependent basis  $\{\mathbf{e}_\rho, \mathbf{e}_\chi, \mathbf{n}\}$  with  $\mathbf{e}_\chi = \mathbf{n} \times \mathbf{e}_\rho$  we formulate the skyrmion Ansatz  $\mathbf{m} = \sin \Theta(\rho)[\mathbf{e}_\rho \cos \Phi_0 + \mathbf{e}_\chi \sin \Phi_0] + \cos \Theta(\rho)\mathbf{n}$ . Here,  $\Theta(\rho)$  is the skyrmion profile in a planar film where the constant  $\Phi_0$  determines the skyrmion type. That is,  $\Phi_0 = 0, \pi$  and  $\Phi_0 = \pm\pi/2$  correspond to a Néel and a Bloch skyrmion, respectively. The Ansatz used here assumes that  $\mathbf{m} = \pm\mathbf{n}$  at a large distance from the center of the skyrmion. The latter means that we neglect the curvature-induced deviation of the ground state from the normal direction, which is generally<sup>37</sup> of the order  $\mathcal{O}(\ell^2 \kappa_\alpha^2, \ell^2 \kappa_1 \kappa_2)^{13}$ . Here  $\ell = \sqrt{A_{ex}/K}$  is the exchange length with  $A_{ex}$  and  $K$  being the exchange stiffness and the coefficient of the easy-normal anisotropy, respectively.

Using the GPC- Ansatz, in the linear order of the principal curvatures, we obtain the gyro- and damping-tensors as in a planar film, namely  $G_{\alpha\beta} = \epsilon_{\alpha\beta} G$  with  $G = 4\pi N_{\text{top}} M_s \hbar / \gamma$  and  $D_{\alpha\beta} = \delta_{\alpha\beta} D$  with  $D = 4\pi \mathcal{C}_0 M_s \hbar / \gamma$ . Here,  $N_{\text{top}} = \frac{1}{2} [\cos \Theta(0) - \cos \Theta(\infty)] = \pm 1$  is the skyrmion topological charge, and the dimensionless constant  $\mathcal{C}_0 = \frac{1}{4} \int_0^\infty [\Theta'^2 + \rho^{-2} \sin^2 \Theta] \rho d\rho$  is determined by the skyrmion profile. The CCD is as follows

$$D_{\alpha\beta}^u = -4\pi \frac{\hbar M_s}{\gamma} \mathcal{C}_1 \hat{R}_{\alpha\gamma} h_{\gamma\beta} \quad (3)$$

where  $\hat{R}_{\alpha\beta} = \delta_{\alpha\beta} \cos \Phi_0 + \epsilon_{\alpha\beta} \sin \Phi_0$  is the rotation matrix,  $h_{\alpha\beta} = h_{\alpha\beta}(X^1, X^2)$  are elements of the shape operator in the skyrmion center, and  $\mathcal{C}_1 = \frac{1}{4} \int_0^\infty [\Theta' + \rho^{-1} \sin \Theta \cos \Theta] \rho d\rho$ . Within the framework of the approximations made, we obtain  $G_{\alpha\beta}^u = 0$ . However, taking into account the terms of higher order in the principal curvatures and the curvature-induced deformation of the skyrmion profile can lead to non-zero elements of the tensor  $G_{\alpha\beta}^u$ .<sup>38</sup>

We now compute the curvature-induced correction of the skyrmion energy for the case of interfacial DMI:  $\Delta E_{\text{Néel}} = -8\pi \hbar (\cos \Phi_0 A_{ex} \mathcal{C}_1 - D_{\text{DM}} \mathcal{C}_2) \mathcal{H}(X^1, X^2) + \mathcal{O}(\kappa_1^2, \kappa_2^2, \kappa_1 \kappa_2)$  (See details in SI). Here,  $D_{\text{DM}}$  is the DMI constant, and  $\mathcal{C}_2 = \frac{1}{4} \int_0^\infty \sin^2 \Theta \rho d\rho$ . Thus, we reproduce the result previously obtained<sup>21,25</sup> for a coarser Ansatz of a skyrmion on a curved surface. For an Néel skyrmion, the flip of the sign of  $D_{\text{DM}}$  flips the sign of  $\cos \Phi_0$ , and therefore flips the sign of  $\Delta E_{\text{Néel}}$ . At the same time, flipping the ground state direction, which is assumed parallel or antiparallel to  $\mathbf{n}$ , does not change  $\Delta E_{\text{Néel}}$ , because both  $\cos \Phi_0$  and  $\mathcal{C}_1$  flip signs in this case.

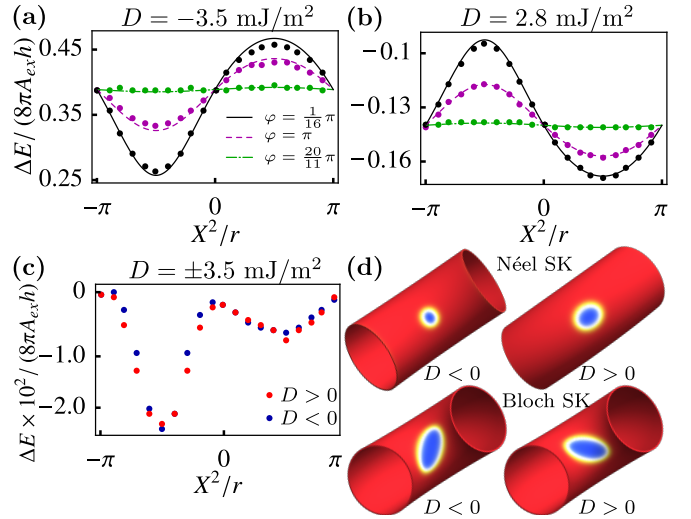


Figure 2. Skyrmion energy as a function of its position. (a) and (b) Show the energy of the Néel skyrmion for different opening angles and  $L = 1130 \text{ nm}$ , (c) shows the energy of the Bloch skyrmion for a fixed opening angle  $\varphi = 20\pi/11$  and  $L = 565 \text{ nm}$ . (d) Shows the skyrmion profile reconstructed from micromagnetic simulations in its equilibrium position: top and bottom rows correspond to the Néel and Bloch skyrmions, respectively, for negative and positive DMI values. Symbols in (a)-(c) correspond to the data obtained by means of numerical simulations, and lines in (a) and (b) correspond to the analytical predictions.

For a Bloch skyrmion, the curvature-dependent energy correction  $\Delta E_{\text{Bloch}} = \mathcal{O}(\kappa_1^2, \kappa_2^2, \kappa_1 \kappa_2)$  is of the second order in the principal curvatures.

*Toroidal surface as a case study*—To illustrate new effects stemming from the current-curvature-induced terms in Eq. (2), we consider the geometry of a bent tube, which is modeled as a section of a torus with length  $L$ , an opening angle  $\varphi$ , a toroidal radius  $R = L/\varphi$ , and a tube radius  $r$ . The tube can be parametrized as  $\boldsymbol{\sigma}(\xi^1, \xi^2) = [R + r \sin(\xi^2/r)] \sin(\xi^1/R) \hat{\mathbf{x}} + [R + r \sin(\xi^2/r)] \cos(\xi^1/R) \hat{\mathbf{y}} + r \cos(\xi^2/r) \hat{\mathbf{z}}$ . Here,  $\xi^1 \in [0, 2\pi R]$  and  $\xi^2 \in [-\pi r, \pi r]$  are the curvilinear coordinates associated with the toroidal and poloidal directions, respectively, as shown in Figs. 1(c) and (d). The chosen parameterization results in the diagonal shape operator  $[h_{\alpha\beta}] = \text{diag}(\kappa_1, \kappa_2)$  with  $\kappa_1 = -R^{-1} \sin \vartheta / (1 + \varrho \sin \vartheta)$  and  $\kappa_2 = -r^{-1}$  being the principal curvatures. Here  $\vartheta = \xi^2/r$  is the poloidal angle and  $\varrho = r/R$ . In this work we focus on the bending-induced effects in the current-driven skyrmion dynamics, absent in the straight cylinder<sup>39,40</sup>.

We begin by analyzing the curvature-induced energy potential. For the chosen geometry, the curvatures depend solely on the poloidal coordinate  $\xi^2$ , see Fig. 1(e,f). As a result, the curvature-induced potential depends only on the skyrmion coordinate  $X^2$ . In Fig. 2(a,b), we compare our analytical prediction  $\Delta E_{\text{Néel}}$  for the Néel skyrmion to the energies extracted from micromagnetic simulations. Our results show a good agreement

between the numerical data and our estimations for  $\Delta E_{\text{Néel}} \propto \mathcal{H}$  obtained in the linear order in  $\kappa_\alpha$ . Thus, the minimum energy is achieved when the Néel skyrmion is on the outer ( $X^2 = \frac{\pi}{2}r$ ) or inner ( $X^2 = -\frac{\pi}{2}r$ ) part of the torus surface for  $D_{\text{DM}} > 0$  or  $D_{\text{DM}} < 0$ , respectively.

Since at this stage our theory does not allow to take into account second-order corrections in  $\kappa_\alpha$ , for Bloch skyrmions we present only numerical data extracted from the simulations<sup>41</sup>, see Fig. 2(c). In contrast to the Néel skyrmion, we observe that the energy landscape for the Bloch skyrmion is not affected by the sign of  $D_{\text{DM}}$ . A Bloch skyrmion has two equilibrium positions:  $X^2 = \pm \frac{\pi}{2}r$ . However, the global minimum corresponds to the inner position  $X^2 = -\frac{\pi}{2}r$ , where the Gaussian curvature reaches its extreme negative value, as shown in Fig. 1(e). This later is intrinsically related to the winding-number selection of solitonic magnetic textures in curved systems<sup>16-18,42</sup> and to curvature-induced magnetochirality<sup>43,44</sup>. Note that  $N_{\text{top}} = -1$  for the considered skyrmions. Fig. 2(d) shows the images of Néel and Bloch skyrmions relaxed in their equilibrium positions. For the Bloch skyrmion, the amplitude of the energy landscape is two orders of magnitude lower than that of the Néel skyrmion. To extract the curvature-induced energy of the Bloch skyrmion from the simulations, we significantly increase the curvature. The latter results in the noticeable elliptical deformation of the skyrmion shape<sup>24,25</sup>, as illustrated in Fig. 2(d). In the following, we will consider only Néel skyrmions.

For the torus, the curvature-induced force  $\mathbf{F} = F_2 \mathbf{e}_2$  has only one component  $F_2 = 8\pi h \Xi r^{-1} \partial_\vartheta \kappa_1$ , where  $\Xi = A_{ex} \mathcal{C}_1 - D_{\text{DM}} \mathcal{C}_2$ . Here and in what follows, we address the case  $D_{\text{DM}} > 0$  and  $\cos \Phi_0 = 1$ . Note that constants  $\Xi$  and  $\mathcal{C}_n$  are uniquely determined by the dimensionless DMI constant  $d = D_{\text{DM}} / \sqrt{A_{ex} K}$  or by skyrmion radius (see Fig. S3 and Ref. [25]). We will apply the current in the toroidal direction  $\mathbf{u} = u^1 \mathbf{e}_1$ , which is technically accessible and convenient for the analysis. In this case, the Thiele Eqs. (2) can have a steady-state solution  $V^1 = u^1 + F_2(\vartheta_0)/G$ ,  $V^2 = 0$ , where the poloidal angle of the skyrmion position  $\vartheta_0 = X_0^2/r$  is determined by the equation

$$\alpha F_2(\vartheta_0) = G u^1 \left[ \beta \frac{D_{11}^u(\vartheta_0)}{D} + \beta - \alpha \right]. \quad (4)$$

For the simplest hypothetical case  $u^1 = 0$  and  $\alpha = 0$ , Eq. (4) is turned into an identity and the skyrmion velocity  $V^1 = F_2(\vartheta_0)/G$  is determined solely by the initial skyrmion coordinate  $\vartheta_0$ , which can be arbitrary. The frequency of the toroidal skyrmion motion is  $\Omega = \Omega_0 \cos \vartheta_0 / (1 + \varrho \sin \vartheta_0)^3$ , where  $\Omega_0 = -\frac{\gamma \Xi}{N_{\text{top}} M_s} \frac{1}{2\pi R^2 r}$ . In the limit  $\varrho \ll 1$ ,  $\Omega$  reaches its maximal values  $\Omega_{\text{max}} \approx \Omega_0$  and  $\Omega_{\text{max}} \approx -\Omega_0$  for  $\vartheta_0 \approx -3\varrho$  and  $\vartheta_0 \approx -\pi + 3\varrho$ , respectively. This corresponds to the almost extreme top or bottom skyrmion positions, with a tiny shift towards the inner part of the torus.

For the particular case  $\alpha = \beta$ , Eq. (4) is reduced to  $\cot \vartheta_0 / (1 + \varrho \sin \vartheta_0) = u^1 / u_0$ , which has a solution for

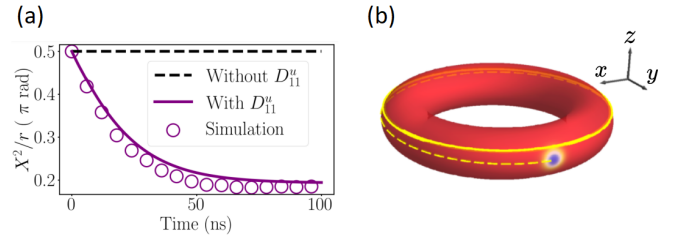


Figure 3. Skyrmion trajectory for  $\alpha = \beta = 0.5$ ,  $|J| = 10 \times 10^{12}$  A/m<sup>2</sup>,  $\varphi = 2\pi$ , and  $L = 1130$  nm. (a) Skyrmion position as a function of time. Purple line and circle depict the trajectory predicted by the analytical model (line) and micromagnetic simulations (circles). The black-dashed line shows the skyrmion trajectory in the absence of the CCD. (b) depicts the skyrmion trajectory along the bent tube. The dashed line shows the trajectory during the first 50 ns.

any current,  $u^1$ , value. Here  $u_0 = 4\pi\Omega_0 \mathcal{C}_0 R^2 / \mathcal{C}_1$ . In the limit  $\varrho \ll 1$ , the skyrmion velocity is

$$V^1 \approx u^1 \left[ 1 + \frac{\mathcal{C}_1}{2\mathcal{C}_0 R} \frac{1}{\sqrt{1 + (u^1/u_0)^2}} \right]. \quad (5)$$

In the limit of large currents  $|u^1| \gg |u_0|$ , one obtains  $V^1 \approx u^1 + V_g$ , where  $V_g = 2\pi R \Omega_0$  is the correction stemming from the geometrically induced potential. As the current increases, the skyrmion reaches the top ( $\vartheta_0 \rightarrow 0$ ) or bottom ( $\vartheta_0 \rightarrow \pm\pi$ ) trajectory. It depends on the signs of  $u^1$ ,  $u_0$ , as well as on the initial skyrmion position. The described skyrmion dynamics is essentially determined by the new term  $D_{11}^u$ ; its crucial role is illustrated in Fig. 3. In a flat system, the condition  $\alpha = \beta$  suppresses the transverse motion from the standard skyrmion Hall effect in a flat system<sup>45</sup>. However, in our case, there is a velocity component perpendicular to the current direction. The skyrmion's transverse velocity  $\dot{X}^2$  vanishes only at a new steady position. Results for a nanotube with  $r = 50$  nm,  $L = 1130$  nm, and  $\varphi = 2\pi$  are shown in Fig. 3. The skyrmion starts its motion at  $X^2/r = 0.5$  and propagates toward a new steady state defined by the balance between the CIF and the effective force originated from the CCD term. During the transient propagation, the skyrmion exhibits a velocity transverse to the current direction, as evidenced by its poloidal displacement represented by the red line shown in Fig. 3(a). The skyrmion position in time is sketched in the schematic representation given in Fig. 3(b). Without current-curvature effects this initial transverse motion would not occur, as shown by the black-dashed line in Fig. 3(a). To validate the analytical findings, we have performed micromagnetic simulations using the TetMag code<sup>46</sup> under identical initial conditions (details of simulations are given in SI). Our results, shown by purple circles, confirm the emergence of an extra Hall effect stemming from current-curvature coupling in curved geometries.

For the general case  $\alpha \neq \beta$ , Eq. (4) can only be resolved for certain parameter values, meaning that a

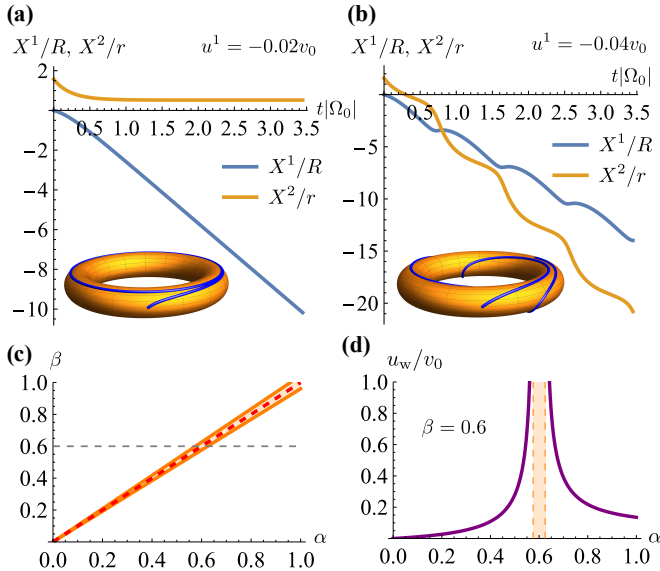


Figure 4. Comparison of the translational and oscillatory skyrmion motions is shown in panels (a) and (b), respectively. Here, we consider a torus with  $R = 10\ell$  and  $r = 2\ell$ , and a skyrmion with  $N_{\text{top}} = -1$  with radius  $R_s = 0.5\ell$ . These parameters correspond to  $V_g \approx -0.027v_0$  with  $v_0 = \gamma\sqrt{A_{\text{ex}}K}/M_s$ , and  $\Omega_0 \approx -4.3 \times 10^{-4}\gamma K/M_s$ . For  $\alpha = 0.1$  and  $\beta = 0.3$  we obtain  $\Upsilon \approx 0.062$  and estimate from (6)  $u_w \approx 0.0271v_0$ . The exact value numerically obtained from (2) is  $u_w \approx 0.0286v_0$ . For the considered values of  $R$ ,  $r$ , and  $R_s$ , the condition  $\Upsilon > 1$  is shown on panels (c) and (d) by the orange shadowing. The dependence  $u_w(\alpha)$  determined by Eq. (6) is shown on panel (d) for fixed  $\beta = 0.6$ .

translational skyrmion motion is not always possible. Instead, a skyrmion can experience an oscillatory dynamics, during which it performs periodic rotations in the poloidal direction. The condition for the transition from one type of dynamics to another is more complex than the conventional Walker breakdown<sup>32,47</sup> induced by the spin-transfer torque. However, it can be easily analyzed in the limit  $\varrho \ll 1$ . In this limit, the translational motion occurs for any value of the applied current, if  $\Upsilon = \frac{\beta}{|\alpha - \beta|} \frac{|\mathbf{c}_1|}{c_0 R} > 1$ . For  $\Upsilon < 1$ , the translational motion occurs only if the current does not exceed some critical value (Walker limit):  $|u^1| < u_w$ , where

$$u_w = 2|V_g| \frac{\alpha}{|\alpha - \beta|} \frac{1}{\sqrt{1 - \Upsilon^2}}. \quad (6)$$

The translational and the oscillatory motions are com-

pared in Fig. 4(a,b). For a straight cylinder ( $R \rightarrow \infty$ ), one has  $V_g = 0$ ,  $\Upsilon = 0$  and consequently  $u_w = 0$ . In this case, the translational motion occurs only under the condition  $\alpha = \beta$ . This is consistent with previous results<sup>39,40</sup>. A direct consequence of the new CCD term  $D_{11}^u$  is the change in the condition of a guaranteed translational motion, namely  $\Upsilon > 1$ , instead of the condition  $\alpha = \beta$  relevant for the planar systems<sup>32</sup>. Within the plane  $(\alpha, \beta)$ , the condition  $\Upsilon > 1$  determines a 2D area surrounding the line  $\alpha = \beta$ , as illustrated in Fig. 4(c). The critical velocity  $u_w$  becomes infinitely large at the boundary of the region determined by the condition  $|\Upsilon| = 1$ , see Fig. 4(d).

*Conclusions.*— We generalized the Thiele equation for the case of the current-driven skyrmion dynamics along a thin curvilinear film. We demonstrated that curvature-induced modification of the spin-transfer torques results in two additional terms in the Thiele equation, namely the symmetric  $D_{\alpha\beta}^u$  and antisymmetric  $G_{\alpha\beta}^u$  tensors. Within the approximations used (linear order in the principal curvatures and neglecting curvature-induced skyrmion deformation), the antisymmetric tensor vanishes. However, its presence may be important for more accurate models of skyrmions or for the Thiele dynamics of other topological solitons. As an example, we considered the motion of a skyrmion along a toroidal surface and showed that the presence of the tensor  $D_{\alpha\beta}^u$  extends the condition of the Walker limit and leads to the additional Hall effect in the skyrmion dynamics. It is worth mentioning that we have also developed a new framework to describe the skyrmion on a curved surface, based on the geodesic polar coordinates.

*Acknowledgments.*— In Brazil, we thank Capes (Grant N. 001) and INCT/CNPq - Spintrônica e Nanoestruturas Magnéticas Avançadas (INCT-SpinNanoMag), CNPq 406836/2022-1. In Chile we acknowledge CEDENNA under grant CIA250002 from ANID. M. Castro acknowledges Proyecto ANID Fondecyt Postdoctorado 3240112. V.K. acknowledges financial support by the Deutsche Forschungsgemeinschaft (DFG, German Research Foundation) through the Würzburg-Dresden Cluster of Excellence ctd.qmat – Complexity, Topology and Dynamics in Quantum Matter (EXC 2147, project-id 390858490). K.Y. acknowledges financial support from the Deutsche Forschungsgemeinschaft (DFG, German Research Foundation) under grant No. YE 232/2-1.

<sup>1</sup> N. D. Mermin, *Rev. Mod. Phys.* **51**, 591 (1979).

<sup>2</sup> S.-S. Chern and J. Simons, *Annals of Mathematics* **99**, 48 (1974).

<sup>3</sup> D. D. Sheka, O. V. Pylypovskiy, O. M. Volkov, K. V. Yershov, V. P. Kravchuk, and D. Makarov, *Small* **18**, 2105219 (2022).

<sup>4</sup> D. D. Sheka, *Applied Physics Letters* **118**, 230502 (2021).

<sup>5</sup> D. Makarov, O. M. Volkov, A. Kákay, O. V. Pylypovskiy, B. Budinská, and O. V. Dobrovolskiy, *Advanced Materials* **34**, 2101758 (2022).

<sup>6</sup> R. Streubel, P. Fischer, F. Kronast, V. P. Kravchuk, D. D. Sheka, Y. Gaididei, O. G. Schmidt, and D. Makarov, *J.*

- Phys. D: Appl. Phys. **49**, 363001 (2016).
- <sup>7</sup> D. Makarov and D. Sheka, eds., *Curvilinear Micromagnetism: From Fundamentals to Applications*, Topics in Applied Physics, Vol. 146 (Springer International Publishing, 2022).
  - <sup>8</sup> O. Bezsmertna, R. Xu, O. Pylypovskyi, D. Raftrey, A. Sorrentino, J. A. Fernandez-Roldan, I. Soldatov, D. Wolf, A. Lubk, R. Schäfer, P. Fischer, and D. Makarov, *Nano Letters* **24**, 15774 (2024).
  - <sup>9</sup> D. Sanz-Hernández, A. Hierro-Rodriguez, C. Donnelly, J. Pablo-Navarro, A. Sorrentino, E. Pereiro, C. Magén, S. McVitie, J. M. de Teresa, S. Ferrer, P. Fischer, and A. Fernández-Pacheco, *ACS Nano* **14**, 8084 (2020).
  - <sup>10</sup> R. M. Corona, E. Saavedra, S. Castillo-Sepulveda, J. Escrig, D. Altbir, and V. L. Carvalho-Santos, *Nanotechnology* **34**, 165702 (2023).
  - <sup>11</sup> S. Castillo-Sepúlveda, R. Cacilhas, V. L. Carvalho-Santos, R. M. Corona, and D. Altbir, *Phys. Rev. B* **104**, 184406 (2021).
  - <sup>12</sup> V. P. Kravchuk, D. D. Sheka, A. Kákay, O. M. Volkov, U. K. Röbller, J. van den Brink, D. Makarov, and Y. Gaididei, *Phys. Rev. Lett.* **120**, 067201 (2018).
  - <sup>13</sup> Y. Gaididei, V. P. Kravchuk, and D. D. Sheka, *Phys. Rev. Lett.* **112**, 257203 (2014).
  - <sup>14</sup> K. V. Yershov, V. P. Kravchuk, D. D. Sheka, and U. K. Röbller, *SciPost Phys.* **9**, 043 (2020).
  - <sup>15</sup> V. P. Kravchuk, U. K. Röbller, O. M. Volkov, D. D. Sheka, J. van den Brink, D. Makarov, H. Fuchs, H. Fangohr, and Y. Gaididei, *Phys. Rev. B* **94**, 144402 (2016).
  - <sup>16</sup> S. Vojkovic, V. L. Carvalho-Santos, J. M. Fonseca, and A. S. Nunez, *Journal of Applied Physics* **121**, 113906 (2017).
  - <sup>17</sup> O. M. Volkov, O. V. Pylypovskyi, F. Porrati, F. Kronast, J. A. Fernandez-Roldan, A. Kákay, A. Kuprava, S. Barth, F. N. Rybakov, O. Eriksson, S. Lamb-Camarena, P. Makushko, M.-A. Mawass, S. Shakeel, O. V. Dobrovolskiy, M. Huth, and D. Makarov, *Nat. Commun.* **15**, 2193 (2024).
  - <sup>18</sup> B. Miranda-Silva, P. H. C. Taveira, A. W. Teixeira, J. M. Fonseca, L. N. Rodrigues, R. G. Elías, A. Riveros, N. Vidal-Silva, and V. L. Carvalho-Santos, *Phys. Rev. B* **105**, 104430 (2022).
  - <sup>19</sup> R. G. Elías, N. Vidal-Silva, and V. L. Carvalho-Santos, *Scientific Reports* **9**, 14309 (2019).
  - <sup>20</sup> F. Tejo, D. Toneto, S. Oyarzún, J. Hermosilla, C. S. Danna, J. L. Palma, R. B. da Silva, L. S. Dorneles, and J. C. Denardin, *ACS Applied Materials & Interfaces* **12**, 53454 (2020).
  - <sup>21</sup> A. Korniienko, A. Kákay, D. D. Sheka, and V. P. Kravchuk, *Phys. Rev. B* **102**, 014432 (2020).
  - <sup>22</sup> A. G. Silva-Junior, J. M. Fonseca, J. I. Costilla, M. M. Amaral, A. Riveros, and V. L. Carvalho-Santos, *Journal of Applied Physics* **136**, 043902 (2024).
  - <sup>23</sup> V. L. Carvalho-Santos, R. G. Elias, J. M. Fonseca, and D. Altbir, *Journal of Applied Physics* **117**, 17E518 (2015).
  - <sup>24</sup> A. Bichs, K. V. Yershov, and V. P. Kravchuk, *Low Temperature Physics* **51**, 550 (2025).
  - <sup>25</sup> K. V. Yershov, A. Kákay, and V. P. Kravchuk, *Phys. Rev. B* **105**, 054425 (2022).
  - <sup>26</sup> A. A. Thiele, *Phys. Rev. Lett.* **30**, 230 (1973).
  - <sup>27</sup> V. L. Carvalho-Santos, M. A. Castro, D. Salazar-Aravena, D. Laroze, R. M. Corona, S. Allende, and D. Altbir, *Applied Physics Letters* **118**, 172407 (2021).
  - <sup>28</sup> W. Farias, I. Santece, and P. Coura, *Journal of Magnetism and Magnetic Materials* **568**, 170386 (2023).
  - <sup>29</sup> K. V. Yershov, V. P. Kravchuk, D. D. Sheka, O. V. Pylypovskyi, D. Makarov, and Y. Gaididei, *Phys. Rev. B* **98**, 060409 (2018).
  - <sup>30</sup> G. H. R. Bittencourt, D. Gálvez-Poblete, M. Castro, D. Altbir, A. S. Nunez, S. Allende, and V. L. Carvalho-Santos, *Nano Futures* **9**, 025001 (2025).
  - <sup>31</sup> G. H. R. Bittencourt, M. Castro, A. S. Nunez, D. Altbir, S. Allende, and V. L. Carvalho-Santos, *Nanoscale* **16**, 16844 (2024).
  - <sup>32</sup> A. Thiaville, Y. Nakatani, J. Miltat, and Y. Suzuki, *Europhysics Letters (EPL)* **69**, 990 (2005).
  - <sup>33</sup> S. Zhang and Z. Li, *Physical Review Letters* **93**, 127204 (2004).
  - <sup>34</sup> D. D. Sheka, V. P. Kravchuk, and Y. Gaididei, *Journal of Physics A: Mathematical and Theoretical* **48**, 125202 (2015).
  - <sup>35</sup> D. D. Sheka, V. P. Kravchuk, D. Peddis, G. Varvaro, M. Krupiński, M. Albrecht, D. Erb, S. Facsko, and D. Makarov, in *Curvilinear Micromagnetism*, Vol. 146, edited by D. Makarov and D. Sheka (Springer Nature Switzerland, 2022).
  - <sup>36</sup> Supplemental materials containing details of the analytical calculations and micromagnetic simulations. Link to be given by APS.
  - <sup>37</sup> This deviation appears not for all surfaces.
  - <sup>38</sup> Note that in this case, Thiele equation (2) can have a more general form, as presented in Eq.(S.5) of SI<sup>36</sup>.
  - <sup>39</sup> W. Wang, P. Hu, L. Kong, D. Song, and H. Du, *Phys. Rev. B* **107**, 134407 (2023).
  - <sup>40</sup> X. Wang, X. S. Wang, C. Wang, H. Yang, Y. Cao, and P. Yan, *Journal of Physics D: Applied Physics* **52**, 225001 (2019).
  - <sup>41</sup> All simulations have the following common parameters:  $r = 50$  nm,  $h = 2$  nm,  $A_{ex} = 16 \times 10^{-12}$  J/m,  $K = 5.6 \times 10^5$  J/m<sup>3</sup>,  $M_s = 1.1 \times 10^6$  A/m.
  - <sup>42</sup> V. Vitelli and A. M. Turner, *Phys. Rev. Lett.* **93**, 215301 (2004).
  - <sup>43</sup> K. V. Yershov, V. P. Kravchuk, D. D. Sheka, and Y. Gaididei, *Phys. Rev. B* **92**, 104412 (2015).
  - <sup>44</sup> O. M. Volkov, A. Kákay, F. Kronast, I. Mönch, M.-A. Mawass, J. Fassbender, and D. Makarov, *Phys. Rev. Lett.* **123**, 077201 (2019).
  - <sup>45</sup> Y. Ohki and M. Mochizuki, *Journal of Physics: Condensed Matter* **37**, 023003 (2024).
  - <sup>46</sup> R. Hertel, “tetmag: a finite-element software for general-purpose micromagnetic simulations,” (2023).
  - <sup>47</sup> K. V. Yershov, V. P. Kravchuk, D. D. Sheka, and Y. Gaididei, *Phys. Rev. B* **93**, 094418 (2016).